

Polarization analysis of fluorescence probing the alignment of Xe^+ ions in the resonant Auger decay of the $\text{Xe}^* 4d_{5/2}^{-1}6p$ photoexcited state

M. Meyer,^{1,2} A. Marquette,^{1,2} A. N. Grum-Grzhimailo,^{1,3} U. Kleiman,⁴ and B. Lohmann⁴

¹LURE, Centre Universitaire Paris-Sud, Bâtiment 209D, F-91898 Orsay Cedex, France

²CEA/DRECAM/SPAM, CEN Saclay, F-91105 Gif-sur-Yvette, France

³Institute of Nuclear Physics, Moscow State University, Moscow 119899, Russia

⁴Westfälische Wilhelms-Universität Münster, Institut für Theoretische Physik, Wilhelm-Klemm-Straße 9, D-48149 Münster, Germany

(Received 20 February 2001; published 2 July 2001)

Xe II fluorescence, following the resonant Auger decay of the $\text{Xe}^* 4d_{5/2}^{-1}6p$ photoexcited state, has been measured in the wavelength region $400 \text{ nm} \leq \lambda \text{ (fluor)} \leq 610 \text{ nm}$ by means of dispersed fluorescence spectroscopy, and the degree of linear polarization of the emitted light has been analyzed. From these data, the alignment of the ionic $5p^46p$ states produced by the Auger decay has been determined by taking into account the depolarization of the radiatively decaying Xe II multiplet due to cascade population and hyperfine interactions. Calculations of the alignment are performed in a multiconfigurational Dirac-Fock approach and compared with the experiment. Good agreement between experiment and theory has been obtained for almost all fine-structure components of the Xe II $5p^46p$ multiplet, providing reliable alignment parameters of the ionic states produced upon resonant Auger decay.

DOI: 10.1103/PhysRevA.64.022703

PACS number(s): 32.80.Hd, 32.80.Fb

I. INTRODUCTION

Photoinduced resonant Auger transitions are being extensively investigated at present, benefiting from the development of new synchrotron sources, as well as high-resolution monochromators, and electron spectrometers [1]. As illustrated by numerous articles, the decay of the resonantly photoexcited $\text{Xe}^* 4d^{-1}np$ states represents a showcase for studying the dynamics of the resonant Auger decay. Experimentally, the above resonances can easily and efficiently be excited, and, from a theoretical point of view, the electronic structure of xenon is complex enough to require the incorporation of interesting multielectron phenomena. Methods of electron spectroscopy have been used to study the energy-resolved resonant Auger spectra [2–12] as well as the angular distribution of the Auger electrons [12–17]. Electron-electron coincidences [18], a photoion yield method [19], and observation of the ion fluorescence [20] were utilized to clearly identify the Auger lines and to determine the population pathways of the ion states. By means of spin-resolved electron spectroscopy, the spin polarization of the Auger electrons was measured [21], which enabled a determination of the ratio of complex Auger decay amplitudes for one of the transitions. All these studies have stimulated considerable theoretical efforts to describe the resonant Auger decay in Xe [8–10,17,22–32]. Although sophisticated calculations within relativistic and semirelativistic approaches [10,17,31,32] can satisfactorily reproduce relative intensities and angular distribution parameters for the majority of the Auger lines, there are still sizable discrepancies for some transitions and further studies are necessary to clarify the remaining differences between experiment and theory.

An extension of the above-mentioned studies is the analysis of polarization and/or angular distribution of the fluorescence lines originating from the radiative decay of excited states of the residual Xe II ion after the Auger decay, both in

coincidence with the Auger electron and in noncoincidence modes. Observations of fluorescence in coincidence with the Auger or autoionizing electron can constitute a complete experiment in certain cases [33]. Measurements of polarization and/or angular distribution of fluorescence without detecting the Auger electrons are an important step towards complete information. The importance of measurements of the fluorescence is increasing even now, because, as has been discovered very recently, the dynamical parameters describing the angular distribution and spin polarization of Auger electrons are not independent [34], and observation of only the Auger electron is not enough for a complete characterization of the Auger process. The additional parameter accessible in observing fluorescence (for excitation with linearly polarized light) is the alignment of the ion after the Auger decay. The alignment carries information about the ionization probabilities into different continuum channels, i.e., absolute ratios of the Auger decay amplitudes, since the theoretical description implies a trace over the quantum numbers of the unobserved Auger electrons. In contrast, angular distribution and spin polarization of the Auger electrons normally contain interference between the decay amplitudes. Therefore, a more complete understanding of the dynamics of the Auger decay and a better theoretical description can be achieved by combining information from experiments analyzing Auger electrons and fluorescence.

Observation and spectral analysis of fluorescence photons in the visible wavelength region have certain experimental advantages in comparison with the spectroscopy of Auger electrons, mainly because the fine structure of the residual ion is much more easily resolved by an optical spectrometer than by an electron analyzer. In addition, fluorescence spectra are free from spectral broadening introduced by the exciting photon beam. Furthermore, several fluorescence transitions from the same ionic state can often be observed, providing good possibilities for a cross checking of the mea-

sured alignment. Upon photoexcitation of the $\text{Xe}^* 4d^{-1}6p$ resonances, the dominant relaxation channel is the resonant Auger decay to the $\text{Xe II } 5p^4(^1S, ^1D, ^3P)6p$ and $\text{Xe II } 5p^4(^1S, ^1D, ^3P)7p$ states. Except for the $\text{Xe II } 5p^4(^1S)7p$ levels, all these states are lying below the Xe III threshold and the secondary Auger decay is energetically forbidden. Therefore, studies of the radiative decay of the above Xe II states provide unique direct access to the symmetry and alignment of the formed ions.

The first measurements of the dispersed fluorescence after the resonant Auger decay of the photoexcited $\text{Xe}^* 4d_{5/2}^{-1}6p (J=1)$ state have been performed by Ehresmann *et al.* [20] in the wavelength range between 400 and 550 nm and in the vuv region (90 – 115 nm). They observed the angular distribution of fluorescence lines from the $\text{Xe II } 5p^46p$ levels and they have deduced the alignment of the photoion. In a recent paper, corrected experimental values of the alignment were presented together with a theoretical analysis [32]. Unfortunately, the comparison between the measurements and theoretical predictions was not straightforward, since effects of depolarization of the fine-structure ionic states taking place during their lifetime were not included and no conversion of the observed alignment into the initial value after the Auger decay has been undertaken.

In the present paper, we extend the studies of dispersed fluorescence by analyzing the degree of linear polarization of the fluorescence lines in the spectral range between 400 and 610 nm with improved spectral resolution. Investigations on the angular distribution or the degree of linear polarization of the fluorescence should give equivalent information about the alignment of the Xe II levels. In order to enable a comparison of our data with theoretical predictions for the Auger decay, we have converted the observed alignment into the initial alignment by taking into account the depolarization of the photoion states due to hyperfine interactions and radiative cascades. Furthermore, we have performed calculations for the initial alignment of the $\text{Xe II } 5p^46p$ states after the Auger decay of the $4d_{5/2}^{-1}6p (J=1)$ resonance in a multiconfigurational Dirac-Fock approach and we compare them with the measurements.

The paper is structured as follows. In Sec. II, the experimental setup is briefly described. In Sec. III, we discuss the dispersed fluorescence spectra and their polarization dependence, and deduce the observed alignment of the $\text{Xe II } 5p^46p$ states. A theoretical model is presented in Sec. IV to describe the initial alignment of the $5p^46p$ ionic states after resonant Auger decay. In Sec. V, we establish the link between the observed alignment and the initial alignment after the Auger decay by analyzing the depolarization effects for the radiatively decaying ionic states. Comparison of the experimental and theoretical results is discussed in Sec. VI.

II. EXPERIMENTAL SETUP

The experiments have been performed at the Super-ACO storage ring in Orsay (France) using the monochromatized synchrotron radiation (SR) from the SU6 undulator beamline as the excitation source. The setup for the collection and the spectral analysis of the visible fluorescence light resembles

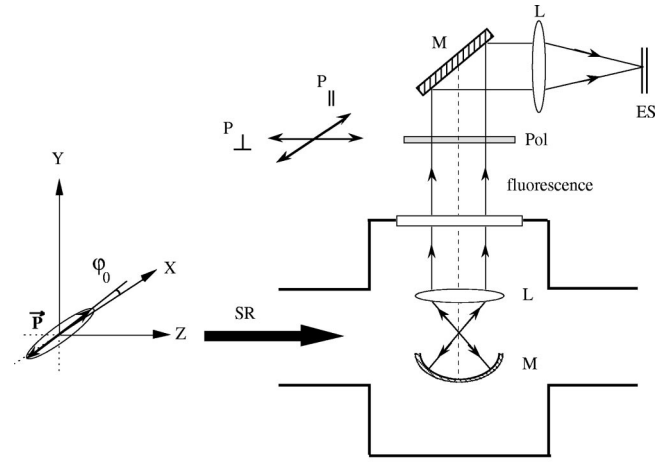


FIG. 1. Scheme of the experimental setup used to determine the degree of linear polarization for fluorescence transitions of Xe ions produced upon resonant $4d \rightarrow 6p$ excitation with synchrotron radiation (SR). The optical elements are indicated: (*M*) mirror, (*L*) lens, (*Pol*) polarizer, and (*ES*) entrance slit of the high-resolution spectrometer. Polarization ellipse of the SR beam is indicated.

closely the one described earlier for the study of the emission following inner-shell excitation of small molecules [35]. The geometry used here for the experiment on atomic Xe is depicted in Fig. 1. Elliptically polarized SR is propagating in the z direction and the main axis of the polarization ellipse is lying close to a fixed x axis with possible deviations in angle φ_0 . The linear polarization of the exciting photon beam has been determined to about 80% by means of angular-resolved photoelectron spectroscopy [36]. The fluorescence photons are produced in the region of interaction between the SR and an effusive Xe gas jet (installed in the x direction and not shown in Fig. 1.) They are collected in the direction perpendicular to the xz plane by a spherical mirror and a convex lens. This arrangement allows us to collect photons within a cone of about 5° opening around the y axis. Outside the experimental chamber, the parallel photon beam passes a commercial sheet polarizer (*Pol*), is deviated by a plane mirror, and is refocused onto the entrance slit of a high-resolution fluorescence spectrometer (Jobin Yvon HR460). Finally, the wavelength-selected photons are registered by a large liquid-nitrogen-cooled CCD detector. The polarizer can be rotated around the y axis and enabled us to record spectra where only the fluorescence light with its polarization vector parallel to the axis of the polarizer is transmitted. The degree of linear polarization P_L of the fluorescence was measured by combining the fluorescence intensities when the axis of the polarizer was directed parallel to the x axis, I_{\parallel} , and perpendicular to it, i.e., parallel to the z axis, I_{\perp} ,

$$P_L = \frac{I_{\parallel} - I_{\perp}}{I_{\parallel} + I_{\perp}}. \quad (1)$$

For a detailed spectral analysis and the assignment of the observed transitions, an 1800 lines/mm grating was used providing a resolution of $\Delta\lambda$ (fluo) = 0.08 nm. The spectra for the investigation of polarization effects and the determina-

tion of the alignment have been recorded with a spectral resolution of $\Delta\lambda$ (flu) = 0.2 nm using a 300 lines/mm grating. Due to its lower dispersion, it is possible to acquire the complete spectral range with only one setting for the position of the grating. Typical count rates have been about 50-100 counts/s in the strongest lines and typical acquisition times have been 30 min for one spectrum. The experimental transmission of the setup has been controlled for the two polarization directions (parallel and perpendicular) by comparing the intensities of fluorescence lines originating from states with angular momentum $J = \frac{1}{2}$, which should show a vanishing degree of polarization. This point will be discussed in some detail in Sec. III B. The production of excited ions $5p^4 6p$ due to direct ionization in the $5s$ or $5p$ shell of Xe has been checked by measuring dispersed fluorescence spectra upon excitation at nonresonant excitation energies. Only very little intensity has been found for radiative transitions from the $5p^4 6p$ levels. This intensity originates dominantly from the cascade population of the $5p^4 6p$ levels from the higher-lying $5p^4 ns$ and $5p^4 nd$ satellite states, whereas the population of the $5p^4 6p$ levels via direct photoionization is small [10]. For the final analysis of the resonant spectra, the intensity of the emission connected with the direct photoionization has been taken into account.

The energy calibration of the exciting SR has been obtained by recording total ion yield spectra in the region around the $4d$ - np resonances and $4d^{-1}$ ionization thresholds. An energy resolution of $\Delta h\nu(\text{SR}) = 50$ meV was used to excite the $\text{Xe}^* 4d_{5/2}^{-1} 6p$ resonance at $h\nu(\text{SR}) = 65.1$ eV.

The background pressure in the experimental chamber was about 7×10^{-8} mbar and was increased up to 5×10^{-5} mbar during the experiment. Xe gas of high purity (99.99%) was used, having the natural composition of Xe isotopes.

III. EXPERIMENTAL RESULTS

A. Dispersed fluorescence spectra

A total of about 108 lines with non-negligible intensity have been observed in the dispersed fluorescence spectra in the wavelength region between 400 nm and 610 nm. All the observed transitions were identified unambiguously according to tabulated data for Xe II [37] and Xe III [38] radiative emissions. The majority of the observed lines can be attributed to the radiative decay of the Xe II $5p^4(^1S, ^1D, ^3P)6p$ multiplet to lower-lying Xe II $5p^4 6s$ or $5p^4 5d$ states. In order to bring out the correspondence as well as the differences between the analysis of Auger electrons and of fluorescence photons, part of the high-resolution fluorescence spectrum covering the wavelength region between 450 nm and 510 nm is displayed in Fig. 2. In addition, a few selected radiative transitions are presented in Table I together with the corresponding data from resonant Auger spectroscopy [10]. The jK notation for the Xe II states from [37] is used throughout the paper; only in the first column of Table I have we also quoted the LSJ terms in order to facilitate the comparison with the Auger data. A more comprehensive list of observed radiation transitions from the Xe II $5p^4 6p$ levels will be presented below (Table II) in the analysis of fluorescence polarization.

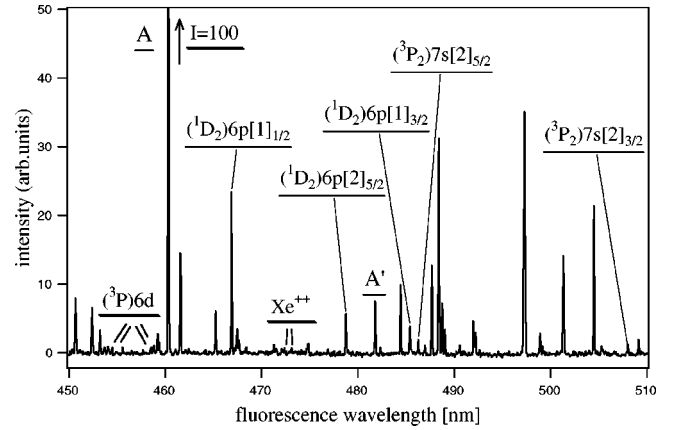


FIG. 2. Part of the dispersed fluorescence spectrum obtained upon excitation of the $\text{Xe}^* 4d_{5/2}^{-1} 6p$ resonance using high spectral resolution [$\Delta\lambda$ (flu) = 0.08 nm]. Some of the lines are labeled by the initial state of the radiative transition (for details, see the text and Table II).

An important difference in the results obtained by the Auger spectroscopy and the fluorescence spectroscopy shows up in the fact that the same ionic state appearing as a single Auger line gives rise to several fluorescence lines. For example, in the investigated wavelength region, the radiative decay of the excited Xe II $5p^4(^1D_2)6p[2]_{3/2}$ and $6p[2]_{5/2}$ states results in five and six observed fluorescence lines, respectively, with different intensities (see Table I). Similarly, the strong line at λ (flu) = 460.3 nm (labeled “A” in Fig. 2) is related to the radiative transition $\text{Xe II } 5p^4(^3P_2)6p[1]_{3/2} \rightarrow 5p^4(^3P_2)6s[2]_{3/2}$, while the same initial state also gives rise to the weak line at λ (flu) = 481.8 nm (labeled “A’”) attributed to the transition to the $5p^4(^3P_2)5d[2]_{3/2}$ state. For a fixed initial ionic state, the relative intensities are determined by the corresponding optical transition probabilities. In contrast, relative intensities of the fluorescence lines originating from different initial ionic states are governed by the relative population of these states and, therefore, are correlated with the strengths of the corresponding Auger transitions. For example, fluorescence lines attributed to decays of the $6p$ levels are generally much stronger than those connected with the $7s$ levels (cf. Fig. 2), in accordance with the relative strength of the $6p$ and $7s$ Auger lines in the electron spectra.

Even more important is the difference in energy resolution when comparing electron and fluorescence spectroscopy. All five Auger lines given in Table I are part of a group of lines, which are not completely resolved in the electron spectra of [10] with a total kinetic-energy resolution of about $\Delta E_{\text{kin}} = 50$ meV. The two fine-structure components $\text{Xe II } 5p^4(^1D_2)6p[2]_{5/2}$ and $5p^4(^1D_2)6p[2]_{3/2}$, separated by only 34 meV (cf. Table I), are not distinguishable in the electron spectra. In the fluorescence analysis (Fig. 2), the corresponding lines appear well separated at λ (flu) = 478.80 nm [$5p^4(^1D_2)6p[2]_{5/2} \rightarrow 5p^4(^3P_1)5d[2]_{3/2}$] and 485.35 nm [$5p^4(^1D_2)6p[2]_{3/2} \rightarrow 5p^4(^3P_1)5d[2]_{3/2}$]. In fact, all five Auger lines in Table I, in particular the weak Xe II $5p^4(^3P_2)7s$ lines, are hardly resolved in the electron spectra [10], but can be clearly distinguished by dispersed fluo-

TABLE I. Comparison between results obtained by means of resonant Auger electron and dispersed fluorescence spectroscopy. For the Xe II states, the $5s^25p^4$ configuration of the ionic core has always been left out. The jK notation is taken from Ref. [37].

Initial ionic state	Electron spectrum, Ref. [10]		Fluorescence spectrum, this work		
	Kinetic energy (eV)	Relative intensity	Final ionic state	λ (fluo) (nm)	Relative intensity
$(^1D_2)6p[2]_{3/2}$ $(^1D)6p\ ^2D_{3/2}$	36.621	70	$(^3P_0)5d[2]_{3/2}$	407.32	30
			$(^3P_1)5d[1]_{3/2}$	416.20	226
			$(^1D_2)6s[2]_{5/2}$	447.10	242
			$(^3P_1)5d[2]_{3/2}$	485.35	246
			$(^1D_2)6s[2]_{3/2}$	526.15	1662
$(^1D_2)6p[2]_{5/2}$ $(^1D)6p\ ^2D_{5/2}$	36.587	77	$(^3P_1)5d[3]_{7/2}$	420.34	50
			$(^1D_2)6s[2]_{5/2}$	441.49	1385
			$(^3P_1)5d[2]_{3/2}$	478.80	360
			$(^3P_1)5d[2]_{5/2}$	512.57	320
			$(^1D_2)6s[2]_{3/2}$	518.40	299
			$(^3P_1)5d[3]_{5/2}$	572.62	697
			$(^3P_2)6p[2]_{5/2}$	486.20	121
$(^3P_2)7s[2]_{5/2}$ $(^3P)7s\ ^4P_{5/2}$	36.550	6.2	$(^3P_2)6p[3]_{7/2}$	531.36	100
			$(^3P_1)5d[1]_{3/2}$	402.43	313
$(^1D_2)6p[1]_{1/2}$ $(^1D)6p\ ^2P_{1/2}$	36.521	102	$(^3P_1)5d[2]_{3/2}$	466.86	1484
			$(^3P_2)7s[2]_{3/2}$	467.40	42
$(^3P)7s\ ^2P_{3/2}$	36.474	6.7	$(^3P_2)6p[2]_{3/2}$	467.40	42
			$(^3P_2)6p[3]_{5/2}$	507.98	81

rescence spectroscopy. In the present experiment, it was possible to disentangle unambiguously all fine-structure components of the Xe II $5p^4(^1S_0, ^1D_2, ^3P_{0,1,2})6p[K]_J$ multiplet. The used spectral resolution of $\Delta\lambda$ (fluo) = 0.08 nm would correspond to a kinetic-energy resolution of $\Delta E_{\text{kin}} = 0.5$ meV in the resonant Xe* $4d_{5/2}^-16p$ Auger spectrum. Only recently could the Xe II $5p^46p$ states be completely resolved by means of very high-resolution electron spectroscopy [11] using the high brilliance of a third-generation synchrotron radiation source and its high photon-energy resolution, which enables studies under extreme resonant Raman conditions. The energy resolution in this experiment has been estimated to about $\Delta E_{\text{kin}} = 10$ meV.

The main drawback of fluorescence studies on excited ions produced upon inner-shell excitation is related to possible effects of radiation cascades, which distort the population and polarization of the initial states of the measured optical transitions [39,40]. The radiation cascades might develop in many steps via different intermediate states and, therefore, can lead to the emission of several photons. In the present case of Xe ions produced upon resonant $4d \rightarrow 6p$ excitation, the Auger decay leads not only to the Xe II $5p^46p$ states, but also to the higher-lying states, mainly to $5p^47p$ levels caused by the shakeup process and also quite efficiently to some of the $5p^47s$ and $5p^46d$ levels formed by the conjugate shakeup process. The corresponding electron transitions manifest themselves as satellite lines in the resonant Auger spectra [10]. Therefore, an additional population of Xe II $5p^46p$ states via a radiative cascade is possible. For example, up to 8.5% of the relative population of the configuration $5p^46p$ arises from the cascade decay of the configuration $5p^47p$ according to a configuration-average estimate [32]. For the individual $5p^46p$ multiplet levels, the

population by cascade processes can be much larger. Fluorescence transitions from the Xe II $5p^47p$ levels to the lower-lying $6d$ or $7s$ levels have not been observed in our measurements, because they give rise to emission in the wavelength region λ (fluo) > 610 nm [37]. But we could clearly identify some lines attributed to the decays Xe II $5p^47s \rightarrow 5p^46p$ [e.g., the lines at λ (fluo) = 486.2 nm, 508.1 nm, and 509.2 nm in Fig. 2] as well as to the decays Xe II $5p^46d \rightarrow 5p^46p$ [e.g. several lines around λ (fluo) = 454 nm and 458 nm]. For the determination of the initial population and the initial alignment of the Xe II $5p^46p$ states formed upon the resonant Auger decay, the possibility of cascading has to be taken into account in the analysis of the fluorescence data for each fine-structure level of the $5p^46p$ configuration.

B. Polarization of fluorescence

The experimental determination of the alignment of the Xe II $5p^46p$ states, which are produced after the resonant Auger decay, was obtained by measuring the degree of linear polarization P_L for the observed fluorescence lines according to Eq. (1). The results are presented in Table II, where the transitions are ordered according to the initial state. The relative intensities are normalized arbitrarily by setting the intensity of the strongest line in the spectrum at λ (fluo) = 460.26 nm to 100. The corresponding fluorescence spectra are displayed in Fig. 3(a) for the wavelength region between 500 and 545 nm. The spectra have been recorded with the axis of the polarizer oriented parallel (dotted line, direction P_{\parallel} in Fig. 1) and perpendicular (solid line, direction P_{\perp} in Fig. 1) to the polarization vector of the SR light. As for these measurements, the spectral resolution was slightly reduced [$\Delta\lambda$

TABLE II. Radiative transitions from the Xe II $5p^46p$ ionic states observed upon excitation to the Xe* $4d_{5/2}^{-1}6p$ resonance. The relative intensities are taken from the high-resolution spectra (cf. Fig. 2). The numbering of initial states is according to Ref. [17]. Intensities are normalized to the strong (3P_2) $6p[1]_{3/2} \rightarrow (^3P_2)6s[2]_{3/2}$ transition at λ (fluo) = 460.26 nm, for which the intensity was arbitrarily set to 100. The initial states with $J = \frac{1}{2}$ cannot be aligned. The most reliable values of the observed alignment are indicated with bold type.

No.	Initial state	Final state	λ (fluo) (nm)		Intensity	P_L	$\mathcal{A}_{20}^o(J)$
			[37]	This work			
1	$(^3P_2)6p[2]_{3/2}$	$(^3P_2)6s[2]_{5/2}$	533.933	533.93	4.5	+0.016(33)	-0.12(25)
		$(^3P_2)6s[2]_{3/2}$	597.646	597.60	2.0	-0.044(62)	-0.08(11)
2	$(^3P_2)6p[2]_{5/2}$	$(^3P_2)6s[2]_{5/2}$	529.222	529.21	22.7	+0.178(10)	+0.32(2)
		$(^3P_2)5d[2]_{5/2}$	603.620	603.60	2.1	+0.166(76)	+0.30(14)
		$(^3P_2)5d[3]_{7/2}$	605.115	605.05	3.5	-0.111(70)	+0.60(37)
3	$(^3P_2)6p[3]_{5/2}$	$(^3P_2)6s[2]_{3/2}$	541.915	541.88	33.4	-0.273(10)	+0.50(2)
		$(^3P_2)5d[3]_{7/2}$	553.107	553.08	3.0	-0.146(48)	+0.78(25)
		$(^3P_2)5d[2]_{3/2}$	571.961	571.94	2.7	-0.262(61)	+0.49(11)
4	$(^3P_2)6p[1]_{1/2}$	$(^3P_2)6s[2]_{3/2}$	537.239	537.22	6.7	-0.036(38)	
		$(^3P_2)5d[2]_{3/2}$	566.756	566.77	2.7	-0.054(62)	
		$(^3P_2)5d[1]_{1/2}$	594.553	594.48	1.2	-0.028(61)	
5	$(^3P_2)6p[3]_{7/2}$	$(^3P_2)6s[2]_{5/2}$	484.433	484.40	9.9	+0.069(25)	-0.16(6)
		$(^3P_2)5d[3]_{7/2}$	547.261	547.22	0.9	-0.176(130)	-0.29(20)
6	$(^3P_2)6p[1]_{3/2}$	$(^3P_2)6s[2]_{3/2}$	460.303	460.26	100	-0.045(15)	-0.08(3)
		$(^3P_2)5d[2]_{5/2}$	467.456	467.40	3.5	+0.026(45)	-0.19(34)
		$(^3P_2)5d[2]_{3/2}$	481.802	481.77	7.5	-0.054(25)	-0.10(5)
7	$(^3P_0)6p[1]_{1/2}$	$(^3P_2)5d[1]_{1/2}$	424.388	424.36	1.5	-0.020(60)	
		$(^3P_0)6s[0]_{1/2}$	519.137	519.12	7.9	+0.018(35)	
8	$(^3P_1)6p[0]_{1/2}$	$(^3P_2)5d[1]_{1/2}$	411.041	410.89	3.2	-0.009(28)	
		$(^3P_1)6s[1]_{3/2}$	543.896	543.85	5.0	+0.005(25)	
9	$(^3P_0)6p[1]_{3/2}$	$(^3P_0)6s[0]_{1/2}$	488.353	488.31	31.2	+0.061(8)	-0.09(1)
		$(^3P_1)6s[1]_{3/2}$	530.927	530.90	5.3	-0.043(20)	-0.08(4)
10	$(^3P_1)6p[2]_{5/2}$	$(^3P_1)6s[1]_{3/2}$	492.148	492.14	2.9	-0.005(25)	+0.01(5)
11	$(^3P_1)6p[2]_{3/2}$	$(^3P_0)6s[0]_{1/2}$	452.421	452.41	6.5	+0.092(38)	-0.14(6)
		$(^3P_1)6s[1]_{3/2}$	488.730	488.67	7.1	+0.032(22)	+0.06(4)
12	$(^3P_1)6p[1]_{3/2}$	$(^3P_1)6s[1]_{3/2}$	465.194	465.23	6.1	+0.104(48)	+0.20(9)
		$(^3P_1)5d[1]_{1/2}$	498.877	498.82	2.8	-0.131(45)	+0.19(6)
		$(^3P_2)5d[0]_{1/2}$	545.045	545.02	2.0	-0.120(64)	+0.17(9)
		$(^3P_1)6s[1]_{1/2}$	575.103	575.06	4.1	-0.161(42)	+0.23(6)
13	$(^3P_1)6p[1]_{1/2}$	$(^3P_1)5d[1]_{1/2}$	491.966	491.95	4.6	-0.004(28)	
		$(^3P_2)5d[0]_{1/2}$	536.807	536.75	1.6	-0.011(51)	
		$(^3P_1)6s[1]_{1/2}$	565.938	565.93	3.5	-0.033(44)	
14	$(^1D_2)6p[3]_{5/2}$	$(^3P_1)5d[1]_{3/2}$	476.905	476.94	0.5	0.00(10)	0.00(20)
		$(^3P_1)5d[2]_{3/2}$	569.961	569.91	0.3	-0.003(100)	+0.01(20)
15	$(^1D_2)6p[1]_{3/2}$	$(^3P_2)5d[1]_{3/2}$	410.495	410.49	3.0	-0.009(82)	-0.02(15)
		$(^3P_2)5d[0]_{1/2}$	421.469	421.42	18.3	+0.041(18)	-0.06(3)
		$(^3P_0)5d[2]_{3/2}$	448.595	448.60	2.5	-0.076(85)	-0.14(15)
		$(^3P_0)5d[2]_{5/2}$	461.550	461.54	14.5	+0.020(21)	-0.15(16)
		$(^1D_2)6s[2]_{5/2}$	497.271	497.29	35.0	+0.028(6)	-0.21(5)
		$(^3P_1)5d[2]_{5/2}$	589.329	589.34	6.0	-0.011(26)	+0.08(19)
16	$(^1D_2)6p[3]_{7/2}$	$(^1D_2)6s[2]_{3/2}$	597.113	597.09	6.6	-0.039(34)	-0.07(6)
		$(^3P_0)5d[2]_{5/2}$	453.249	453.24	0.9	+0.178(110)	-0.42(27)
17	$(^1D_2)6p[2]_{3/2}$	$(^3P_1)5d[1]_{3/2}$	416.216	416.20	3.6	+0.066(100)	+0.12(19)
		$(^1D_2)6s[2]_{5/2}$	447.090	447.10	3.7	-0.022(64)	+0.16(47)
		$(^3P_1)5d[2]_{3/2}$	485.377	485.35	3.8	+0.082(45)	+0.16(9)
		$(^1D_2)6s[2]_{3/2}$	526.195	526.15	26.2	+0.067(6)	+0.13(1)

TABLE II. (*Continued*).

No.	Initial state	Final state	λ (fluo) (nm)		Intensity	P_L	$\mathcal{A}_{20}^o(J)$
			[37]	This work			
18	$(^1D_2)6p[2]_{5/2}$	$(^1D_2)6s[2]_{5/2}$	441.484	441.49	21.8	+0.185(19)	+0.34(4)
		$(^3P_1)5d[2]_{3/2}$	478.777	478.80	5.7	-0.198(38)	+0.37(7)
		$(^3P_1)5d[2]_{5/2}$	512.570	512.57	5.0	+0.221(26)	+0.41(5)
		$(^1D_2)6s[2]_{3/2}$	518.448	518.40	4.7	-0.201(37)	+0.38(7)
		$(^3P_1)5d[3]_{5/2}$	572.691	572.62	11.0	+0.198(15)	+0.36(3)
19	$(^1D_2)6p[1]_{1/2}$	$(^3P_1)5d[1]_{3/2}$	402.519	402.43	4.9	+0.015(35)	
		$(^3P_1)5d[2]_{3/2}$	466.849	466.86	23.4	0	
20	$(^1S_0)6p[1]_{1/2}$	$(^1D_2)5d[1]_{3/2}$	413.881	413.85	0.2	-0.020(100)	
		$(^1S_0)6s[0]_{1/2}$	526.831	526.82	0.8	+0.056(95)	
21	$(^1S_0)6p[1]_{3/2}$	$(^1D_2)5d[1]_{1/2}$	450.711	450.70	7.9	+0.131(51)	-0.20(8)
		$(^1S_0)6s[0]_{1/2}$	501.283	501.32	14.1	+0.078(10)	-0.12(2)

(fluo) = 0.2 nm]; a high-resolution spectrum is added in Fig. 3(b) for comparison and to allow for a better wavelength calibration. Some of the lines show clearly considerable changes of their relative intensities, while others are almost unaffected by the change of polarization. Possible polarization-dependent differences in the optical transmissions of the setup for the two polarization directions have been corrected by normalizing the spectra to the same intensity for the line at λ (fluo) = 466.86 nm (not shown in Fig. 3), which is due to a transition Xe II $5p^4(^1D_2)6p[1]_{1/2}$

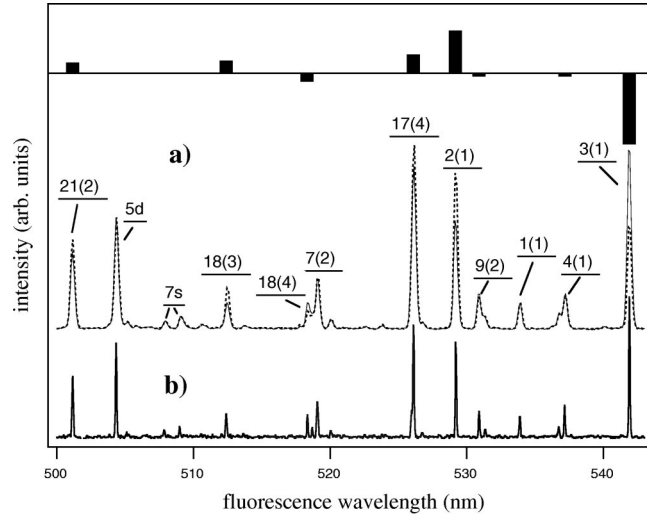


FIG. 3. (a) Part of the dispersed fluorescence spectra obtained upon excitation of the Xe* $4d_{5/2}^{-1}6p$ resonance with the axis of the polarizer directed parallel (dotted line) and perpendicular (solid line) to the polarization vector of the exciting synchrotron radiation. The spectral resolution in the fluorescence analysis was set to $\Delta\lambda$ (fluo) = 0.2 nm. The differences in intensity of the individual lines are given separately as a histogram on top of the figure. Transitions are labeled according to the initial Xe II $5p^46p$ states introduced in Table II, while the numbers in parentheses refer to the ordering with respect to the final states in the same table. (b) High-resolution fluorescence spectrum [$\Delta\lambda$ (fluo) = 0.08 nm] shown for a clearer identification of the observed transitions.

$\rightarrow 5p^4(^3P_1)5d[2]_{3/2}$. For initial states with total angular momentum $J = \frac{1}{2}$, no polarization effect can be observed and the intensity in both spectra has to be the same. In the row spectra, a difference of less than 5% in the total intensity was found, indicating an almost polarization-independent transmission. The validity and correctness of this normalization procedure are demonstrated by the results for the other fluorescence lines originating from states with $J = \frac{1}{2}$ (cf. states 4, 7, 8, 13, 19, and 20 in Table II), which all show a vanishing small degree of polarization within the estimated error bars.

Most of the other transitions from the Xe II $5p^46p$ states are characterized by a pronounced effect of polarization. (Remember that the values of P_L given in Table II correspond to 80% polarization of the SR.) In general, the degree of polarization is found to be quite high for transitions from initial levels having high J values, but the sign of P_L can be different for different final states of the fluorescence transitions. The latter is related to the fact that the degree of polarization P_L for the fluorescence transitions depends on the initial as well as on the final state. To demonstrate the consistency of our data already at this level, transitions from the same Xe II $5p^46p$ multiplet state and to final states with the same total angular momentum J_f have to be compared. For example, the two transitions from $(^3P_2)6p[2]_{5/2}$ leading to $J_f = \frac{5}{2}$ (see the initial state 2 in Table II) show the same large positive polarization, whereas the transition to the $J_f = \frac{7}{2}$ final state has a negative sign. Similar examples can be observed for other initial states (e.g., states 6, 12, and 18). Some of the lines, mainly those with quite low intensity, show larger error bars than the given value for the polarization degree. These lines can only give a tendency and indicate the limit of our experimental precision.

In order to deduce from the polarization data, which are values specific to the fluorescence transitions, a more general quantity characterizing the physical process of interest, i.e., the Auger decay, we have determined the alignment of the corresponding initial ionic states. The alignment $\mathcal{A}_{20}(J)$ of the Xe II $5p^46p$ states produced upon the resonant Auger decay represents a link to the theoretical treatment of the Auger decay (see below). The observed alignment $\mathcal{A}_{20}^o(J)$ is

given by the relation (e.g., [41], p. 121)

$$\mathcal{A}_{20}^o(J) = \frac{1}{\alpha_2} \frac{2P_L}{P_L - 3} \quad (J \geq 1), \quad (2)$$

where the coefficient α_2 is defined by

$$\alpha_2 = (-1)^{J+J_f+1} \sqrt{\frac{3}{2}} \sqrt{2J+1} \begin{Bmatrix} 1 & 1 & 2 \\ J & J & J_f \end{Bmatrix}. \quad (3)$$

J and J_f represent the total angular momenta of the initial and final state of the fluorescence transition, respectively. The standard notation for the Wigner $6j$ symbol is used. Note that the alignment $\mathcal{A}_{20}^o(J)$ in Eq. (2) is taken in the coordinate system with the z axis parallel to the electric field of the linearly polarized SR. For comparison with other measurements and with theory, the alignment observed in our experiment with elliptically polarized SR has to be transformed to the alignment parameter of the photoion for the case of pure linearly polarized SR. Since the spatial symmetry in observing the polarization of fluorescence in the case of the resonant Auger process is identical to the corresponding measurements on direct photoionization and resonance fluorescence, we can use known equations [41,42] to account for the not complete polarization of the SR. With definition (1) and the geometry displayed in Fig. 1, the degree of linear polarization of fluorescence P_L in Eq. (2) should be transformed according to

$$P_L \rightarrow \frac{2P_L}{P_L(1 - P_l \cos 2\varphi_0) + (1 + P_l \cos 2\varphi_0)}. \quad (4)$$

Here P_l is the degree of linear polarization of the SR and φ_0 is the azimuth angle of its principal polarization axis. The value of P_L is insensitive to small deviations of φ_0 from 0, as is the case in our experiments [36].

The values for the alignment (2) with the correction (4) are summarized in the last column of Table II. We introduced additional errors for $\mathcal{A}_{20}^o(J)$ due to uncertainties in the value of $P_l = 0.80 \pm 0.05$. The data show now a much greater consistency than the data for P_L , i.e., the values for the alignment extracted from different fluorescence lines originating from the same ion level are, within the error bars, in good accordance. In order to make further comparison easier, we have indicated the most reliable values with bold-type characters. The criteria have been the intensity of the lines and the position of the lines in the spectrum, i.e., the possibility to separate them completely from other close-lying transitions. In the rest of the discussion, only these values will be used.

IV. THEORY

The theoretical description of the alignment of the ion after the resonant Auger decay utilizes the two-step model, in our case well justified experimentally [43]: first, the resonant Auger state is photoexcited,

$$\gamma + A(J_0) \rightarrow A^*(J_i),$$

which decays during the second step by ejection of the Auger electron,

$$A^*(J_i) \rightarrow A^+(J) + e_A.$$

We denote by J_0 and J_i the total angular momenta of the initial and photoexcited atomic states, respectively. Standard methods of statistical tensor formalism can be used to express the alignment of the ion $A^+(J)$ in terms of the Auger decay amplitudes [41]. Implying the dipole approximation for the photoexcitation by linearly polarized light and taking into account the vanishing angular momentum J_0 for the initial atomic state, we arrive at

$$\mathcal{A}_{20}(J) = \sqrt{6(2J+1)} \sum_{lj} (-1)^{J+j} \begin{Bmatrix} 1 & 1 & 2 \\ J & J & j \end{Bmatrix} \frac{\Gamma_{lj}}{\Gamma}, \quad (5)$$

where

$$\Gamma_{lj} = 2\pi \langle J, \varepsilon l j; J_t = 1 || V || J_i = 1 \rangle^2 \quad (6)$$

are the partial Auger widths in the channel with the orbital and total angular momenta, l and j , of the Auger electron; ε is the energy of the Auger electron; the total angular momentum of the intermediate photoexcited state is fixed to $J_i = 1$; J_t is the total angular momentum of the final state, $\mathbf{J}_t = \mathbf{J} + \mathbf{j}$; and $\Gamma = \sum_{lj} \Gamma_{lj}$ is the total Auger decay width to the given ionic state $A^+(J)$. Equation (5) is a particular case of a well-known expression from the theory of polarization transfer [44].

For obtaining the numerical data of the partial Auger decay widths Γ_{lj} , we apply a relativistic distorted-wave approximation. Here, the bound-state wave functions of the initial photoexcited $\text{Xe}^* 4d_{5/2}^{-1}6p_{3/2}$ ($J_i = 1$) state and the final $\text{Xe II } 5p^46p$ states are constructed using the multiconfigurational Dirac-Fock (MCDF) computer code of Grant *et al.* [45]. Intermediate coupling has been taken into account with the mixing coefficients determined in the average level calculation mode. The calculation of the Auger transition matrix elements is done applying a relaxed orbital method. Thus, the bound electron orbitals of the $4d_{5/2}^{-1}6p_{3/2}$ ($J_i = 1$) state are calculated in the field of the excited atom. On the other hand, the bound electron orbitals of the final state are calculated in the field of the singly ionized atom. While a single configuration approach has been used for the calculation of $4d_{5/2}^{-1}6p_{3/2}$ ($J_i = 1$), the atomic state function of the singly ionized final state $|p, \pi J\rangle$ with the total angular momentum J and parity π is constructed as a linear combination of jj -coupled configuration state functions (CSFs),

$$|p, \pi J\rangle = \sum_{k=1}^{n_p} c_k^p |\gamma_k, \pi J\rangle. \quad (7)$$

The label p numerates the states for distinction. The label γ_k denotes the occupation of the different subshells and their angular couplings, while c_k^p ($k = 1, 2, \dots, n_p$) are the mixing coefficients for the state p . The configuration states $|\gamma_k, \pi J\rangle$

are constructed from antisymmetrized products of Dirac orbitals, which are eigenstates of the total (one-electron) angular momentum and parity.

To form the possible $5p^4(^3P)6p$, $5p^4(^1D)6p$, and $5p^4(^1S)6p$ final states, we included 13 CSFs occurring for Auger transitions with a spectator Rydberg electron, i.e., $6p_{3/2} \rightarrow 6p_{3/2}$ transitions, as well as eight CSFs resulting from the so-called spin-flip transitions $6p_{3/2} \rightarrow 6p_{1/2}$. Thus, a total of 21 CSFs have been considered in Eq. (7).

The continuum wave function of the Auger electron is evaluated by solving the Dirac equation with an intermediate coupling potential, which is constructed from the mixed CSF of the final ionic state. Thereby, we take into account that the ejected Auger electron moves within the field of the residual ion. A local energy-dependent potential [46] was introduced to account for electron exchange between the continuum and the bound states. With this approximation, the transition matrix elements, and thus the partial Auger widths (6), are obtained for calculating the relevant alignment parameters (5).

Our approach goes beyond the spectator model used in previous calculations of angular distribution and spin-polarization parameters [14,23,24] by fully taking into account the variation of the intermediate ionic charge cloud through the excited Rydberg electron. It further exceeds a more recent investigation of angular distribution and spin polarization in resonant Auger transitions [25,26] by taking into account also the eight CSFs resulting from the spin-flip transitions. Most recently, this approach has been applied for a detailed theoretical analysis of the spin-flip transition of the angle- and spin-resolved resonantly excited $\text{Xe}^*(6p_{3/2})\text{N}_5\text{O}_{23}\text{O}_{23}$ Auger spectrum [47].

Before comparing the calculated and the measured values of the alignment of the photoion, $\mathcal{A}_{20}(J)$ and $\mathcal{A}_{20}^o(J)$, the effects of depolarization of the ionic states taking place during their radiative lifetime have to be considered.

V. DEPOLARIZATION EFFECTS

With respect to the present experimental conditions, there are mainly two depolarization effects that have to be taken into account for the determination of the alignment for the $\text{Xe II } 5p^4 6p$ levels formed after the resonant Auger decay, namely the hyperfine interactions and the fluorescence cascades.

A. Depolarization due to hyperfine interactions

The natural isotope mixture of Xe consists of approximately 26% of the isotope ^{129}Xe with nuclear spin $I = \frac{1}{2}$, 21% of ^{131}Xe with $I = \frac{3}{2}$, and other isotopes with vanishing nuclear spin [48]. The hyperfine splitting of the $\text{Xe II } 5p^4 6p$ states in the ^{129}Xe and ^{131}Xe isotopes is of the order of $10^2 - 10^3$ MHz [49]. As the Auger decay width is much larger than this splitting, the hyperfine structure levels are populated coherently during the Auger decay. The nuclear spin is unpolarized immediately after the Auger process and its polarization is not observed. Therefore, to account for the depolarization due to a precession of the angular momentum \mathbf{J} of the electronic shell of the ion about the total angular

momentum $\mathbf{F} = \mathbf{J} + \mathbf{I}$, depolarization factors can be introduced similar to the cases of direct photoionization and electron-impact excitation [41,50,51],

$$\mathcal{A}_{20}^h(J) = G_2(J) \mathcal{A}_{20}(J). \quad (8)$$

Here $\mathcal{A}_{20}^h(J)$ is the alignment reduced by the hyperfine interactions, $\mathcal{A}_{20}(J)$ is the alignment before the depolarization is taken into account, and $G_2(J)$ is the depolarization factor. The widths of the $5p^4 6p$ states are determined by the radiation lifetime of 5–10 ns [37,52], and therefore are in the range 15–30 MHz, which is much smaller than the hyperfine level separation. For this case, the depolarization factor takes the simple form

$$G_2(J) = (2I+1)^{-1} \sum_F (2F+1)^2 \begin{Bmatrix} F & F & 2 \\ J & J & I \end{Bmatrix}^2, \quad (9)$$

where the summation runs over all possible values F for a given fine-structure level with the total angular momentum J of the electronic shell. For the isotope mixture, the depolarization factor given in Eq. (9) should be weighted according to the abundances of the isotopes. Taking particular values of the angular momenta I and J and the natural isotope mixture of Xe, we determine the following depolarization factors for the Xe II fine-structure states: $G_2(J = \frac{3}{2}) = 0.75$, $G_2(J = \frac{5}{2}) = 0.83$, and $G_2(J = \frac{7}{2}) = 0.89$.

B. Depolarization due to radiation cascades

Depolarization effects due to the radiation cascade from higher-lying levels is usually very difficult to analyze, because often many pathways are possible and not all of them are completely known with respect to their transition probabilities as well as to the population and alignment of the initial states of the cascades [40]. The $5p^4 6p$ levels of Xe II formed upon resonant Auger decay can additionally be populated by radiation cascades via the states with configurations $5p^4 7s$ and $5p^4 6d$, as well as via the highest states of the $5p^4 5d$ configuration. The polarization of fluorescence lines belonging to the transitions from these states to the levels of the $5p^4 6p$ configuration was found to be negligible in our experiment. This is confirmed, for example, by the lines labeled $5d$ and $7s$ in Fig. 3, which show no polarization dependence and which are attributed to transitions from $5p^4(^1S_0)5d[2]_{5/2}$, $5p^4(^3P_2)7s[2]_{3/2}$, and $5p^4(^1D_2)7s[2]_{5/2}$ excited states. Therefore, the radiative decay to the $6p$ states can be considered as isotropic. The vanishing small polarization of the above lines can be caused by a combination of a few factors: a loss of ionic alignment due to a sharing of polarization between the unobserved photon and the residual ion in the first step of the cascades from the $7p$ states (e.g., [41], p. 130); depolarization due to the hyperfine interactions existing in each ionic state involved in the cascades; mutual compensation of the alignments introduced by several radiation transitions to the same fine structure $5p^4 7s, 6d, 5d$ from different fine-structure $5p^4 7p$ states, as well as by the conjugate shakeup Auger transitions, which populates the $7s$, $6d$, and $5d$ states directly; and al-

ready small or zero initial alignment of particular $7p$ states contributing to the population of the $7s$, $6d$, and $5d$ states by the radiation transitions. Introducing the isotropic model simplifies considerably the description of the depolarization effect due to cascades in two respects. First, the depolarization of a given $5p^4 6p[K]_J$ fine-structure level can be described by an identical increase of population for all its magnetic substates. Similar to the case of the isotropic contributions into the anisotropic x-ray lines induced by particle impact ionization [53], this leads to the simple relation

$$\mathcal{A}_{20}^c(J) = D(J) \mathcal{A}_{20}(J) \quad (10)$$

with the depolarization cascade factor

$$D(J) = \frac{W^A(J)}{W^A(J) + W^c(J)}. \quad (11)$$

Here $\mathcal{A}_{20}^c(J)$ is the alignment reduced by the cascade, and $W^A(J)$ and $W^c(J)$ stand for the population probabilities of the fine-structure level formed directly by the Auger decay and by the fluorescence cascade, respectively. Secondly, the two depolarization mechanisms, due to the hyperfine interactions and due to cascades, are completely independent, because they affect the statistical tensors of different ranks, i.e., the additional isotropic population of the $5p^4 6p$ levels arising from the cascade changes only the zero rank tensor, while the hyperfine interactions affect only tensors with non-zero ranks (see the Appendix for more details). As a result, for the observed alignment, it follows from Eqs. (8) and (10) that

$$\mathcal{A}_{20}^o(J) = D(J) G_2(J) \mathcal{A}_{20}(J), \quad (12)$$

where now the depolarization factors $D(J)$, Eq. (11), have to be calculated in an appropriate model.

C. Calculation of depolarization cascade factors

Not all transition probabilities, which are needed to analyze the radiation cascades in Xe II and to determine the depolarization factors $D(J)$, Eq. (11), are known from the literature. The data for the $7p \rightarrow 7s$ and $7p \rightarrow 6d$ transitions [54] are especially scarce and not reliable enough to calculate the cascades of interest, which incorporate thousands of pathways. Therefore, in order to find the depolarization factors, we performed extended calculations within an intermediate-coupling multiconfigurational Hartree-Fock approximation using the MCHF package of Froese Fischer *et al.* [55]. The atomic model used in these calculations is briefly outlined below.

Within the MCHF approach, LS-coupled wave functions are used as the basis in the multiconfiguration expansion (7):

$$|p, \pi J\rangle = \sum_{k=1}^{N_p} C_k^p | \gamma_k, \pi L_k S_k \rangle, \quad (13)$$

where L_k and S_k stand for the orbital angular momentum and the spin of the CSF, respectively. To find the electron orbitals, we started with the term-average calculation for the

$5s^2 5p^4 6p$ configuration of Xe II and then generated physical $n\ell$ orbitals in the frozen-core term-average approximation for the corresponding $5s^2 5p^4 n\ell$ configurations ($n\ell = 6s, 7s, 8s, 7p, 8p, 5d, 6d, 7d, 4f, 5f$). To account additionally for electron correlations, we introduced the pseudo-orbitals $\bar{9}p$, $\bar{9}s$, $\bar{8}d$, and $\bar{9}d$. The pseudo-orbital $\bar{9}p$ was optimized on the energy of the Xe II ground state in the $5p^5 + 5p^4(6p + 7p + 8p + \bar{9}p) + 5p^3 \bar{9}p^2 {}^2P$ calculation with other electron orbitals fixed. The pseudo-orbitals $\bar{9}s$, $\bar{8}d$, and $\bar{9}d$ were optimized in a similar way in the respective calculations $5p^4(6s + 7s + 8s + \bar{9}s) {}^4P$, $5s5p^6 + 5s^2 5p^4(5d + 6d + 7d + \bar{8}d) {}^2S$, and $5p^4(5d + 6d + 7d + \bar{8}d + \bar{9}d) {}^4F$. Then we took the configurations $5s^2 5p^5$, $5s5p^6$, $5s^2 5p^4 6s$, $5s^2 5p^4 7s$, $5s^2 5p^4 6p$, $5s^2 5p^4 7p$, $5s^2 5p^4 5d$, $5s^2 5p^4 6d$, and $5s^2 5p^4 4f$ and generated configurations with single and double replacements of the orbitals in the above set. This new extensive set of configurations was further used in the diagonalization of the Breit-Pauli ionic Hamiltonian. Due to the computational restrictions in the final calculations, we took into account only those configurations γ_k in Eq. (13) for which at least one of the coefficients C_k^p was greater than 0.01 for at least one of the levels p participating in the radiation cascade. Due to a slow convergence of the expansion (13), we had to include, even with this restriction, depending on J , up to $N_p = 1900$ CSFs, which result from 44 configurations for odd Xe II levels and up to $N_p = 2800$ CSFs resulting from 69 configurations for even Xe II levels.

After the wave functions (13) were found, the optical transition probabilities between all discrete fine-structure levels of Xe II were calculated. To find the cascade contributions, a code was written, which uses the output list of transitions from the LSJTR program [56] of the MCHF package as an input and finds the percentage of population of fine-structure levels due to the cascade from a given initial state by the direct summation over all possible pathways. The relative population of the initial states in the cascade was taken from the resonant Auger spectra [10]. There are ambiguities in the assignment of higher-lying Xe II $5p^4 7p, 4f$ and few lower-lying states. This breaks a one-to-one correspondence between an Auger line, which populates an initial level of the cascade, and a calculated level. Although according to our theoretical energies a tentative assignment to some of these final Xe II levels in the Auger decay could be given, we have maintained the ambiguities in the assignment of the levels, which together with known experimental uncertainties in the intensities of the Auger lines [10] results in some “error bars” in the depolarization factors. Thus, having experimental data [10] for relative intensities of the Auger lines and calculating the radiation cascades as described above, we obtain the depolarization factors (11) for each fine-structure Xe II $5p^4 6p[K]_J$ level.

The radiative lifetimes for all fine-structure levels participating in the cascade are produced in the code as a by-product. We used these numbers, as well as the optical transition probabilities, to additionally check the quality of our calculations. For example, our values for the lifetimes of the Xe II $5p^4 6p[K]_J$ fine-structure levels are within the range

TABLE III. Depolarization factors and alignment of the Xe II $5p^46p$ ($J \geq 1$) ionic states upon excitation to the Xe* $4d_{5/2}^{-1}6p$ resonance. Experimental data from Ref. [32] (last column) are corrected with the depolarization factors $D(J)$ and $G_2(J)$ from the present paper.

No.	State	Energy ^a (eV)	$\mathcal{A}_{20}^o(J)$	$D(J)$	$G_2(J)$	$\mathcal{A}_{20}(J)$			
						Expt. this work	Calc. this work	Calc. [32]	Expt. [32]
1	$(^3P_2)6p[2]_{3/2}$	25.991	-0.08(11)	0.53(17)	0.75	-0.20(30)	-0.054	-0.190	-0.07(29)
2	$(^3P_2)6p[2]_{5/2}$	26.012	+0.32(2)	0.67(7)	0.83	+0.58(8)	+0.830	+0.794	+0.71(9)
3	$(^3P_2)6p[3]_{5/2}$	26.204	+0.50(2)	0.77(14)	0.83	+0.79(18)	+0.792	+0.806	+0.80(18)
5	$(^3P_2)6p[3]_{7/2}$	26.228	-0.16(6)	0.53(14)	0.89	-0.34(16)	-0.396	-0.377	-0.17(7)
6	$(^3P_2)6p[1]_{3/2}$	26.609	-0.08(3)	0.96(2)	0.75	-0.11(4)	-0.118	-0.045	-0.12(2)
9	$(^3P_0)6p[1]_{3/2}$	27.211	-0.09(1)	0.88(1)	0.75	-0.14(2)	+0.018	-0.195	-0.08(2)
10	$(^3P_1)6p[2]_{5/2}$	27.394	+0.01(5)	0.27(17)	0.83	+0.04(22)	+0.320	+0.180	+0.21(20)
11	$(^3P_1)6p[2]_{3/2}$	27.412	-0.14(6)	0.95(0)	0.75	-0.20(8)	-0.081	-0.123	-0.07(2)
12	$(^3P_1)6p[1]_{3/2}$	27.540	+0.23(6)	0.94(3)	0.75	+0.32(8)	+0.656	+0.359	+0.15(7)
14	$(^1D_2)6p[3]_{5/2}$	28.109	0.00(20)	0.51(26)	0.83	0.0(5)	+0.503	+0.368	-0.30(32)
15	$(^1D_2)6p[1]_{3/2}$	28.208	-0.21(5)	0.91(1)	0.75	-0.28(6)	+0.484	-0.033	-0.08(5)
16	$(^1D_2)6p[3]_{7/2}$	28.257	-0.42(27)	0.81(12)	0.89	-0.59(39)	-0.297	-0.288	-0.06(6)
17	$(^1D_2)6p[2]_{3/2}$	28.489	+0.13(1)	0.98(1)	0.75	+0.17(2)	+0.060	+0.322	+0.01(4)
18	$(^1D_2)6p[2]_{5/2}$	28.523	+0.36(3)	0.96(3)	0.83	+0.45(4)	+0.517	+0.491	+0.73(5)
21	$(^1S_0)6p[1]_{3/2}$	30.631	-0.12(2)	0.97(0)	0.75	-0.16(2)	-0.200	-0.198	-0.08(2)

^aThe energies of the Xe II $5p^46p$ states were determined using the experimental kinetic energies [12] and the excitation energy of the Xe* $4d_{5/2}^{-1}6p$ ($J=1$) state (65.110 eV).

5.5–9.5 ns; they are mostly larger by 1–2 ns than the values calculated in [37] and agree systematically better with measurements [52].

VI. DISCUSSION

Table III summarizes the data for the observed and initial alignment of the Xe II ion produced upon resonant Auger decay of the photoexcited $4d_{5/2}^{-1}6p$ resonance. The depolarization cascade factors $D(J)$ and the depolarization factors due to the hyperfine interactions $G_2(J)$ are given for individual $5p^46p$ fine-structure states. Our experimental and theoretical results for the initial alignment $\mathcal{A}_{20}(J)$ are compared to data from a complementary study [32]. In the latter, the angular distribution of the fluorescence has been measured, but no corrections for the depolarization effects were introduced in these results. The experimental values given in the last column of Table III are therefore also corrected by the depolarization parameters $D(J)$ and $G_2(J)$ given in columns 5 and 6, respectively.

As expected from the preceding discussion, the values of experimental $\mathcal{A}_{20}(J)$ increase in absolute values with respect to the observed alignment $\mathcal{A}_{20}^o(J)$. Depolarization of the fluorescence lines is generally large: the product of the two depolarization factors $D(J)G_2(J)$ varies in a broad range of 0.2–0.8 when passing from one fine-structure ionic state to another and leads sometimes to corrections in the observed alignment by a factor of 2 or 3 (states 1, 2, 5, and 14) and even more (state 10). These ionic states correspond to the weakest lines in the resonant Auger spectra [10], indicating their small direct population by the Auger decay. Therefore, the strong depolarization of these states due to the cascades is understandable. For some states, the depolarization factors

$D(J)$ show a marked uncertainty due to ambiguities in the Xe II level assignments, as discussed in Sec. V C. Large and different magnitudes of depolarization factors particularly emphasize that a consistent consideration of the depolarization effects for individual ionic states is absolutely necessary. Note that for approximately half of the ionic states, mainly in the lower-energy region of the $5p^46p$ manifold, the depolarization due to the cascades is stronger than that due to the hyperfine interaction, while for the other half of the states the situation is the opposite.

The two sets of experimental data on the ionic alignment $\mathcal{A}_{20}(J)$ are in satisfactory agreement for the majority of states, taking into account rather large error bars for some of them (states 1, 5, 10, and 14). Nevertheless, in some cases the two data sets show clear discrepancies (states 15, 16, 17, 18, and 21). For example, for the states $(^1D_2)6p[1]_{3/2}$ and $(^1D_2)6p[3]_{7/2}$ (15 and 16 in Table III, respectively), the measurements of Lagutin *et al.* [32] show only a small negative alignment, whereas in our experiment some noticeable values (-0.28 and -0.59) were found. The value obtained for line 16 has been deduced from a transition of very small intensity (see Table II), and our error bar, though already large, might still be underestimated. Most of the other discrepancies can be explained by the choice of the reference lines, which is different in both experiments. For example, for lines 15 and 17 we have opted for the most intense transitions (see Table II), whereas in [32] transitions with smaller intensities have been selected due to possible perturbation by overlapping, unresolved transitions of the stronger lines.

To analyze in more detail the relationship between both sets of experimental results with the theoretical predictions, we show in Table IV the results for the partial Auger decay widths, Γ_{ij}/Γ [see Eq. (5)], from the present calculations and

TABLE IV. Calculated relative partial Auger widths and alignment $A_{20}(J)$ of the Xe II $5p^46p$ states.

No.	Final state	Partial decay widths (%)									$A_{20}(J)$		
		$\epsilon s_{1/2}$	$\epsilon d_{3/2}$	This work			[32]			This work	[32]		
				$\epsilon d_{5/2}$	$\epsilon g_{7/2}$	$\epsilon g_{9/2}$	$\epsilon s_{1/2}$	$\epsilon d_{3/2}$	$\epsilon d_{5/2}$	$\epsilon g_{7/2}$	$\epsilon g_{9/2}$		
1	$(^3P)6p^4P_{3/2}$	0.5	15.0	84.4			0.3	1.2	98.5			-0.054	-0.190
2	$(^3P)6p^4P_{5/2}$		0.2	97.9	1.9			3.2	96.0	0.8		+0.830	+0.794
3	$(^3P)6p^2D_{5/2}$		3.1	95.7	1.2			2.3	96.6	1.2		+0.792	+0.806
4	$(^3P)6p^2S_{1/2}$	85.4	14.6				30.1	69.9				0	0
5	$(^3P)6p^4D_{7/2}$			30.7	1.5	67.8			25.4	1.5	73.1	-0.395	-0.377
6	$(^3P)6p^2P_{3/2}$	1.0	9.1	89.9			0.2	15.5	84.3			-0.118	-0.045
7	$(^3P)6p^2P_{1/2}$	30.1	69.9				0.0	100.0				0	0
8	$(^3P)6p^4P_{1/2}$	7.5	92.5				6.9	93.1				0	0
9	$(^3P)6p^2D_{3/2}$	0.0	21.8	78.2			0.0	0.4	99.6			+0.018	-0.195
10	$(^3P)6p^4D_{5/2}$		33.4	66.6	0.0			40.9	57.0	2.1		+0.320	+0.180
11	$(^3P)6p^4S_{3/2}$	0.5	12.3	87.2			0.1	8.1	91.8			-0.081	-0.123
12	$(^3P)6p^4D_{3/2}$	0.1	85.6	14.3			0.1	56.2	43.8			+0.656	+0.359
13	$(^3P)6p^4D_{1/2}$	1.4	98.6				1.4	98.6				0	0
14	$(^1D)6p^2F_{5/2}$		14.1	74.6	11.3			19.1	64.6	16.3		+0.503	+0.368
15	$(^1D)6p^2P_{3/2}$	10.5	76.8	12.7			1.9	18.3	79.8			+0.484	-0.033
16	$(^1D)6p^2F_{7/2}$			2.2	1.4	96.4			1.7	2.0	96.3	-0.297	-0.288
17	$(^1D)6p^2D_{3/2}$	13.7	36.9	49.4			3.3	55.4	41.3			+0.060	+0.322
18	$(^1D)6p^2D_{5/2}$		13.3	75.6	11.0			12.9	73.1	14.0		+0.517	+0.491
19	$(^1D)6p^2P_{1/2}$	78.7	21.3				15.6	84.4				0	0
20	$(^1S)6p^2P_{1/2}$	44.6	55.4				8.3	91.7				0	0
21	$(^1S)6p^2P_{3/2}$	0.0	0.0	100.0			0.0	0.2	99.8			-0.200	-0.198

from the calculations in [32]. Table IV includes also six ionic states $5p^46p$ with $J=\frac{1}{2}$, which are not aligned. The Auger decay into the final $5p^46p$ state with the total angular momentum J gives partial waves ϵlj of the Auger electron with $j=J, J\pm 1$ for $J>\frac{1}{2}$ and two partial waves, $\epsilon s_{1/2}$ and $\epsilon d_{3/2}$, for $J=\frac{1}{2}$.

A close inspection of Table III shows that the two theoretical calculations of the alignment are in good agreement for the $5p^46p$ states with high angular momenta $J=\frac{5}{2}$ and $J=\frac{7}{2}$, while the main discrepancies exist for most of the states with lower angular momentum $J=\frac{3}{2}$. This indicates that the theoretical description of the decay into channels with lower angular momenta of the Auger electron— $\epsilon s_{1/2}$, $\epsilon d_{3/2}$, and $\epsilon d_{5/2}$ —are very sensitive to the details of the theoretical model, which is confirmed by the values of the relative decay widths in Table IV. Indeed, the relative contributions from the $\epsilon s_{1/2}$ and $\epsilon d_{3/2}$ channels to the total decay width differ drastically in the two theoretical models for four out of the six states with $J=\frac{1}{2}$ (states 4, 7, 19, and 20). Similarly, the contributions from the $\epsilon d_{3/2}$ and $\epsilon d_{5/2}$ channels differ strongly in the two models for most of the $5p^46p$ states with $J=\frac{3}{2}$, especially for state 15. In contrast, contributions from the $\epsilon g_{7/2}$ and $\epsilon g_{9/2}$ channels seem rather stable in the calculations. Since the centrifugal barrier does not allow the ϵg electrons to penetrate into the ionic core region, one might deduce that the main source of the disagreement arises from the behavior of the wave functions in the inner atomic region.

Comparing now the values of the alignment in the last four columns of Table III, it is evident that there are further studies needed, both experimental and theoretical, in order to

describe consistently the alignment of all Xe II $5p^46p$ states. The results in all four columns are in very good agreement only for a few states (2, 3, and 11). For states 5, 16, 18, and 21, both calculations give close results in agreement with the present measurements, but disagree with the experimental data from [32]. For states 6 and 17, our calculations are in better agreement with both experiments than the calculations [32], while the calculations [32] are more favorable than the present theoretical results for the states 9, 12, and 15. Note that the five latter states (6, 9, 12, 15, and 17) are the states with the same angular momentum $J=\frac{3}{2}$.

A critical test of the theory could be the study of the orientation of the Xe II $5p^46p$ states, in particular of the multiplet components with $J=\frac{1}{2}$, when the resonant Auger process is induced upon excitation with circularly polarized light. The orientation can be measured by detecting circular polarization of the fluorescence lines observed in the present experiment. The sensitivity of the relative decay width for the $\epsilon s_{1/2}$ and $\epsilon d_{3/2}$ channels to the theoretical model used will result in completely different predictions for the degree of circular polarization of the fluorescence, with particular values depending on the geometry of the setup.

VII. CONCLUSION

The linear polarization of Xe II fluorescence lines has been investigated by means of dispersed fluorescence spectroscopy in the visible wavelength region in the process, when the Xe ions are produced after resonant Auger decay of the photoexcited Xe* $4d_{5/2}^{-1}6p$ state. The observed alignment of the $5p^46p$ ionic states could be related to the initial

alignment induced directly after the Auger decay by accounting for depolarization effects. For most of the $5p^46p[K]_J$ fine-structure levels, the deduced values of the initial alignment are in good agreement with other experimental data derived from the angular distribution of the fluorescence intensity [32], although also few disagreements were found.

Depolarization effects due to hyperfine interaction and radiative cascades have been analyzed theoretically in order to obtain the initial alignment of the $5p^46p$ states. Depolarization is generally large and different for the different fine-structure levels. The analysis shows clearly that reliable and precise alignment parameters can only be determined from fluorescence measurements when the radiative cascades are properly taken into account for individual fine-structure levels, which is an elaborate task for complex atoms. To the best of our knowledge, this is the first time that such a complete analysis has been undertaken for the resonant Auger process. Experimentally, a time-resolved analysis of the fluorescence decay or coincidence measurements between Auger electrons and fluorescence photons have to be used in future studies to show more clearly the importance and influence of the complex radiative cascades.

Calculations of the alignment of the $5p^46p$ states after the resonant Auger decay were performed in the multiconfigurational Dirac-Fock approximation. The derived values for the initial alignment of the $5p^46p$ states are generally in good agreement with the experimental data and with other theoretical estimations [32]. The exception is some fine-structure components with angular momentum $J = \frac{3}{2}$. Our analysis shows that the reason for the disagreement is a very high sensitivity of the partial Auger decay widths in the εs and εd continuum channels to the theoretical model. The presented experimental data on dispersed fluorescence spectroscopy and the resulting determination of the initial alignment of the ionic states formed upon resonant Auger decay demonstrate clearly the importance of these measurements for a detailed verification of advanced theoretical models describing the complicated interactions in many-electron atoms.

ACKNOWLEDGMENTS

We would like to acknowledge Professor W. Mehlhorn and Professor N. Kabachnik for helpful discussions and a careful reading of the manuscript. A.N.G. gratefully acknowledges the hospitality of the LURE Laboratory and of the Université Paris–Sud.

APPENDIX

The observed alignment, which is generally a function of the time window of the detector Δt , is expressed as

$$A_{20}^o(J, \Delta t) = \frac{\int_0^{\Delta t} \rho_{20}(J, t) dt}{\int_0^{\Delta t} \rho_{00}(J, t) dt}. \quad (\text{A1})$$

The statistical tensors $\rho_{k0}(J, t)$ are defined in terms of populations W_M of magnetic substates of the fine-structure level J ,

$$\rho_{k0}(J, t) = C \sum_M (-1)^{J-M} (JM, J-M | k0) W_M(t), \quad (\text{A2})$$

where $(j_1 m_1, j_2 m_2 | j m)$ is the Glebsch-Gordan coefficient; C is a normalization constant. Our experimental conditions imply that the time of observation is much longer than all times typical for the process, including the development of the electromagnetic cascade, and therefore Δt in Eq. (A1) can be set to infinity. We choose the normalization constant C in Eq. (A2) in such a way that the time-integrated statistical tensor $\rho_{00}(J, t)$ gives the total number of ions, which have decayed radiatively from the fine-structure level J during the observation time:

$$\int_0^{\infty} \rho_{00}(J, t) dt = N^A + N^C. \quad (\text{A3})$$

Here N^A and N^C are the total numbers of excited ions at the level J populated by the Auger decay and by the radiative cascades, respectively.

The identical increase of the populations W_M for all magnetic substates of a level with angular momentum J , as is the case in our isotropic model of the cascade, affects only the statistical tensor with the rank $k=0$: it follows from the definition (A2) and the relation $\sum_M (-1)^{J-M} (JM, J-M | k0) = \sqrt{2J+1} \delta_{k0}$. Therefore, only the hyperfine interactions affect the numerator in Eq. (A1), where now the depolarization factor $G_2(J)$ can be separated [41,51],

$$\int_0^{\infty} \rho_{20}(J, t) dt = G_2(J) \rho_{20}^A(J). \quad (\text{A4})$$

Here, we have assumed that the fast Auger process coherently populates the hyperfine structure levels at $t=0$ producing the initial alignment $\rho_{20}^A(J) \equiv \rho_{20}(J, t=0)$. Putting Eqs. (A3) and (A4) into Eq. (A1) and dividing the numerator and the denominator by N^A , we obtain Eq. (12).

-
- [1] G.B. Armen, H. Aksela, T. Åberg, and S. Aksela, *J. Phys. B* **33**, R49 (2000), and references therein.
 [2] W. Eberhardt, G. Kalkoffen, and C. Kunz, *Phys. Rev. Lett.* **41**, 156 (1978).
 [3] V. Schmidt, S. Krummacher, F. Wuilleumier, and P. Dhez,

- Phys. Rev. A* **24**, 1803 (1981).
 [4] S. Southworth, U. Becker, C.M. Truesdale, P.H. Kobrin, D.W. Lindle, S. Owaki, and D.A. Shirley, *Phys. Rev. A* **28**, 261 (1983).
 [5] U. Becker, T. Prescher, E. Schmidt, B. Sonntag, and H.-E.

- Wetzel, Phys. Rev. A **33**, 3891 (1986).
- [6] U. Becker, D. Szostak, M. Kupsch, H.G. Kerkhoff, B. Langer, and R. Wehlitz, J. Phys. B **22**, 749 (1989).
- [7] A. Kivimäki, A. Naves de Brito, S. Aksela, H. Aksela, O.-P. Sairanen, A. Ausmees, S.J. Osborne, L.B. Dantas, and S. Svensson, Phys. Rev. Lett. **71**, 4307 (1993).
- [8] H. Aksela, S. Aksela, G.M. Bancroft, K.H. Tan, and H. Pulkkinen, Phys. Rev. A **33**, 3867 (1986).
- [9] H. Aksela, S. Aksela, O.-P. Sairanen, A. Kivimäki, A. Naves de Brito, E. Nömmiste, J. Tulkki, S. Svensson, A. Ausmees, and S.J. Osborne, Phys. Rev. A **49**, R4269 (1994).
- [10] H. Aksela, O.-P. Sairanen, S. Aksela, A. Kivimäki, A. Naves de Brito, E. Nömmiste, J. Tulkki, A. Ausmees, S.J. Osborne, and S. Svensson, Phys. Rev. A **51**, 1291 (1995).
- [11] G. Öhrwall, J. Bozek, and P. Baltzer, J. Electron Spectrosc. Relat. Phenom. **104**, 209 (1999).
- [12] B. Langer, N. Berrah, A. Farhat, O. Hemmers, and J.D. Bozek, Phys. Rev. A **53**, R1946 (1996).
- [13] T.A. Carlson, D.R. Mullins, C.E. Beall, B.W. Yates, J.W. Taylor, D.W. Lindle, and F.A. Grimm, Phys. Rev. A **39**, 1170 (1989).
- [14] B. Kämmerling, B. Krässig, and V. Schmidt, J. Phys. B **23**, 4487 (1990).
- [15] C.D. Caldwell and S. Hallman, Phys. Rev. A **53**, 3344 (1996).
- [16] N. Berrah and B. Langer, Comments At. Mol. Phys. **33**, 325 (1997).
- [17] H. Aksela, J. Jauhiainen, E. Nömmiste, O.-P. Sairanen, J. Karvonen, E. Kukkk, and S. Aksela, Phys. Rev. A **54**, 2874 (1996).
- [18] E. von Raven, M. Meyer, M. Pahler, and B. Sonntag, J. Electron Spectrosc. Relat. Phenom. **52**, 677 (1990).
- [19] T. Hayaishi, Y. Morioka, Y. Kageyama, M. Watanabe, I.H. Suzuki, A. Mikuni, G. Isoyama, S. Asaoka, and M. Nakamura, J. Phys. B **17**, 3511 (1984).
- [20] A. Ehresmann, H. Schäffer, F. Vollweiler, G. Mentzel, B. Magel, K.-H. Schartner, and H. Schmoranzner, J. Phys. B **31**, 1487 (1998).
- [21] U. Hergenhahn, G. Snell, M. Drescher, B. Schmidtke, N. Müller, U. Heinzmann, M. Wiedenhöft, and U. Becker, Phys. Rev. Lett. **82**, 5020 (1999).
- [22] J.W. Cooper, Phys. Rev. A **39**, 3714 (1989).
- [23] U. Hergenhahn, N.M. Kabachnik, and B. Lohmann, J. Phys. B **24**, 4759 (1991).
- [24] B. Lohmann, J. Phys. B **24**, 861 (1991).
- [25] B. Lohmann, J. Phys. B **32**, L643 (1999).
- [26] B. Lohmann, Aust. J. Phys. **52**, 397 (1999).
- [27] U. Hergenhahn, B. Lohmann, N.M. Kabachnik, and U. Becker, J. Phys. B **26**, L117 (1993).
- [28] U. Hergenhahn and U. Becker, J. Electron Spectrosc. Relat. Phenom. **76**, 225 (1995).
- [29] M.H. Chen, Phys. Rev. A **47**, 3733 (1993).
- [30] S. Fritzsche, Phys. Lett. A **180**, 262 (1993).
- [31] J. Tulkki, H. Aksela, and N.M. Kabachnik, Phys. Rev. A **50**, 2366 (1994).
- [32] B.M. Lagutin, I.D. Petrov, Ph.V. Demekhin, V.L. Sukhorukov, F. Vollweiler, H. Liebel, A. Ehresmann, S. Lauer, H. Schmoranzner, O. Wilhelmi, B. Zimmermann, and K.-H. Schartner, J. Phys. B **33**, 1337 (2000).
- [33] H.-J. Beyer, J.B. West, K.J. Ross, K. Ueda, N.M. Kabachnik, H. Hamdy, and H. Kleinpoppen, J. Phys. B **28**, L47 (1995); K. Ueda, J.B. West, H.-J. Beyer, K.J. Ross, and N.M. Kabachnik, *ibid.* **31**, 4801 (1998), and references therein.
- [34] B. Schmidtke, T. Khalil, M. Drescher, N. Müller, N.M. Kabachnik, and U. Heinzmann, J. Phys. B **33**, 5225 (2000); N.M. Kabachnik and A.N. Grum-Grzhimailo, *ibid.* **34**, L63 (2001).
- [35] A. Marquette, M. Gisselbrecht, W. Bente, and M. Meyer, Phys. Rev. A **62**, 022 513 (2000).
- [36] S. Al-Moussalami, Ph.D. thesis, Université Paris–Sud, 1998.
- [37] J.E. Hansen and W. Persson, Phys. Scr. **36**, 602 (1987).
- [38] W. Persson, C.-G. Wahlström, G. Bertuccelli, H.O. Di Rocco, J.G. Reyna Almandos, and M. Gallardo, Phys. Scr. **38**, 347 (1988).
- [39] H. Hamdy, H.-J. Beyer, J.B. West, and H. Kleinpoppen, J. Phys. B **24**, 4957 (1991).
- [40] J. Jiménez-Mier, C.D. Caldwell, M.G. Flemming, S.B. Whitfield, and P. van der Meulen, Phys. Rev. A **48**, 442 (1993).
- [41] V.V. Balashov, A.N. Grum-Grzhimailo, and N.M. Kabachnik, *Polarization and Correlation Phenomena in Atomic Collisions: A Practical Theory Course* (Kluwer Academic/Plenum Publishers, New York, 2000).
- [42] H. Klar, J. Phys. B **15**, 4535 (1982); W. Kronast, R. Huster, and W. Mehlhorn, Z. Phys. D: At., Mol. Clusters **2**, 285 (1986); H. Hamdy, H.-J. Beyer, J.B. West, and H. Kleinpoppen, J. Phys. B **24**, 4957 (1991); V. Schmidt, Rep. Prog. Phys. **55**, 1483 (1992).
- [43] W. Mehlhorn, in *X-ray and Inner Shell Processes*, edited by T.A. Carlson, M.O. Krause, and S.T. Manson, AIP Conf. Proc. 215 (AIP, New York, 1990), p. 465
- [44] N.M. Kabachnik, in *X-Ray and Inner-Shell Processes*, edited by R.L. Johnson, H. Schmidt-Böcking, and B.F. Sonntag, AIP Conf. Proc. 389 (AIP, Woodbury, New York, 1997), p. 689; N.M. Kabachnik, I.P. Sazhina, and K. Ueda, J. Phys. B **32**, 1769 (1999).
- [45] I.P. Grant, B.J. McKenzie, P.H. Norrington, D.F. Mayers, and N.C. Pyper, Comput. Phys. Commun. **21**, 207 (1980).
- [46] J.B. Furness and I.E. McCarthy, J. Phys. B **6**, 2280 (1973); R. Vanderpoorten, *ibid.* **8**, 926 (1975).
- [47] B. Lohmann and U. Kleiman, in *Many-Particle Spectroscopy of Atoms, Molecules, Clusters and Surfaces*, edited by J. Berakdar and J. Kirschner (Kluwer Academic/Plenum Publishers, London, 2001).
- [48] *CRC Handbook of Chemistry and Physics*, 77th ed. (CRC Press, Boca Raton, 1996–1997), pp 11–82.
- [49] C.R. Bingham, M.L. Gaillard, D.J. Pegg, H.K. Carter, R.L. Mlekodaj, J.D. Cole, and P.M. Griffin, Nucl. Instrum. Methods Phys. Res. **202**, 147 (1982); R.T. Short, S. Mannervik, M. Larsson, P. Sigray, and D. Sonnek, Phys. Rev. A **39**, 3969 (1989), and references therein.
- [50] U. Fano and J.H. Macek, Rev. Mod. Phys. **45**, 553 (1973); C.H. Greene and R.N. Zare, Phys. Rev. A **25**, 2031 (1982).
- [51] K. Blum, *Density Matrix Theory and Applications* (Plenum, New York, 1996).
- [52] V. Fonseca, M. Ortiz, and J. Campos, J. Opt. Soc. Am. **73**, 1070 (1983); L. Ward, A. Wännström, A. Arnesen, R. Hallin, and O. Vogel, Phys. Scr. **31**, 149 (1985); R.E. Mitchell, S.D. Rosner, T.J. Scholl, and R.A. Holt, Phys. Rev. A **45**, 4452 (1992); L. Broström, S. Mannervik, A. Passian, and G. Sundström, *ibid.* **49**, 3333 (1994), and references therein.
- [53] W. Jitschin, H. Kleinpoppen, R. Hippler, and H.O. Lutz, J.

- Phys. B **12**, 4077 (1979); N.M. Kabachnik, V.P. Petukhov, E.A. Romanovskii, and V.V. Sizov, Zh. Éksp. Teor. Fiz. **78**, 1733 (1980) [Sov. Phys. JETP **51**, 869 (1980)].
- [54] I. Martin, C. Hernando, C. Lavin, and A.M. Velasco, J. Quant. Spectrosc. Radiat. Transf. **62**, 71 (1999), and references therein.
- [55] C. Froese Fischer, T. Brage, and P. Jönsson, *Computational Atomic Structure. An MCHF Approach* (IOP Publishing, Bristol, 1997).
- [56] C. Froese Fischer and M.R. Godefroid, Comput. Phys. Commun. **64**, 501 (1991).